# *Weather features drive free-tropospheric baroclinicity variability in the North Atlantic storm track*



Marcheggiani, A. ORCID: https://orcid.org/0000-0002-3571-608X, Dacre, H. ORCID: https://orcid.org/0000-0003-4328-9126, Spensberger, C. ORCID: https://orcid.org/0000-0002-9649-6957 and Spengler, T. ORCID: https://orcid.org/0000-0002-1747-6385 (2025) Weather features drive free-tropospheric baroclinicity variability in the North Atlantic storm track. Quarterly Journal of the Royal Meteorological Society. e5061. ISSN 1477-870X doi: 10.1002/qj.5061 Available at https://centaur.reading.ac.uk/124006/

Received: 26 November 2024 | Revised: 4 June 2025 | Accepted: 1 July 2025

DOI: 10.1002/qj.5061

Quarterly Journal of the Royal Meteorological Society RMetS

RESEARCH ARTICLE

# Weather features drive free-tropospheric baroclinicity variability in the North Atlantic storm track

**Andrea Marcheggiani**[1] | **Helen Dacre**[2] | **Clemens Spensberger**[1] | **Thomas Spengler**[1]

[1]Geophysical Institute, University of Bergen, and Bjerknes Centre for Climate Research, Bergen, Norway

[2]Department of Meteorology, University of Reading, Reading, UK

**Correspondence**
Andrea Marcheggiani, Postdoctoral Fellow, Geophysical Institute, University of Bergen, and Bjerknes Centre for Climate Research, Bergen, Norway.
Email: andrea.marcheggiani@uib.no

**Funding information**
Norwegian Research Council (Norsk Forskningsråd, NFR) via the BALMCAST project (NFR Project 324081); Bjerknes Centre for Climate Research

## Abstract

Despite the fundamental contribution of diabatic processes for the evolution of storm tracks, our theoretical understanding of their role is still incomplete. Given that the strongest diabatic forcing is associated with cyclones, fronts, and atmospheric rivers, these synoptic features must exert a significant influence on the evolution of storm tracks. Their relative contribution to the climatological maintenance of baroclinicity, however, has not been investigated. Hence, we quantify the diabatic contribution of cyclones, fronts, and atmospheric rivers to free-tropospheric baroclinicity variability in the North Atlantic storm track in winter using the isentropic slope framework, which discriminates between diabatic and adiabatic contributions to changes in baroclinicity. The total variability of free-tropospheric baroclinicity within the storm track is characterised by diabatic generation followed by adiabatic decay. We find that the largest diabatic generation of baroclinicity takes place within cyclones, both individually and in combination with fronts, which contribute to more than half of this total variability in the storm track, despite their limited spatial extent and temporal occurrence. The contribution from atmospheric rivers, however, is small, confirming that the presence of moisture alone does not necessarily translate into diabatic production of baroclinicity in the absence of a mechanism for ascent. Though the contribution from the background to the variability is coherent with the total variability, there is no clear synoptic evolution associated with the background variability. Thus, the largest diabatic production of free-tropospheric baroclinicity is tightly linked to cyclones and fronts, whereas its adiabatic depletion occurs irrespective of the presence of weather features.

**KEYWORDS**

baroclinicity, diabatic processes, storm tracks, synoptic features

## 1 | INTRODUCTION

The bulk of the diabatic maintenance of baroclinicity in the free troposphere within storm tracks is provided by latent heating (Chang, 2009; Hoskins & Valdes, 1990; Hotta & Nakamura, 2011; Marcheggiani & Spengler, 2023; Papritz & Spengler, 2015). The majority of this latent heating is associated with large-scale precipitation (Papritz & Spengler, 2015), which has been linked to synoptic weather features, such as extratropical cyclones, fronts, and atmospheric rivers (Konstali *et al.*, 2024). However, despite this close relation, the relative contribution of these weather features to the variability of baroclinicity and storm track activity has not been quantified. Hence, we quantify the contribution of cyclones, fronts, and atmospheric rivers to the total variability in baroclinicity for the North Atlantic storm track.

Whereas extratropical cyclones are primarily thought to reduce meridional temperature gradients and thereby deplete baroclinicity, extratropical cyclones can also effectively restore baroclinicity throughout their evolution via latent heat release associated with precipitation along their trailing cold fronts (Weijenborg & Spengler, 2020). The diabatically generated baroclinicity along the cold front can, in turn, fuel the formation of secondary cyclones (Chaboureau & Thorpe, 1999; Parker, 1998; Rivals *et al.*, 1998), potentially resulting in cyclone clustering (Bjerknes, 1922; Weijenborg & Spengler, 2020). The occurrence of cyclone clustering may then influence the overall intensity and spatial structure of the storm track (Priestley *et al.*, 2020b), further highlighting the importance of moist diabatic processes within synoptic features in regulating the life cycle of storm tracks.

Diabatic processes also play a direct role in shaping atmospheric circulation by influencing the position of the jet stream (Woollings *et al.*, 2016). They anchor the jet to its climatological location in the upstream regions of storm tracks through sensible and latent heat fluxes over western ocean boundary currents (Hotta & Nakamura, 2011; Nakamura *et al.*, 2008; Ogawa & Spengler, 2024). In the free troposphere, on the other hand, latent heating dominates the diabatic contribution (Papritz & Spengler, 2015), intensifying temperature gradients across the jet and thus strengthening the jet itself (Auestad *et al.*, 2024). Given the strong link between moist diabatic processes and synoptic weather features, the latter are expected to play a crucial role in setting the spatial and temporal variability of the jet and of the storm track in general.

Recently, it was highlighted that a better numerical representation of moist dynamics can lead to significant improvements in the representation of location and orientation of storm tracks (Willison *et al.*, 2013; Fuchs *et al.*, 2023; Schemm, 2023; Garfinkel *et al.*, 2024). However, the kind of moist processes that are most crucial in determining the evolution of the storm track are still debated, as different precipitation types (convective and large-scale) can have opposing effects on the position of the jet (Fuchs *et al.*, 2023; Garfinkel *et al.*, 2024) and thus on storm track variability. Several physical mechanisms have been proposed, but none explain either observed or projected storm track shifts (Shaw, 2019). Current climate models still feature significant biases in the representation of mid-latitude storm tracks (Harvey *et al.*, 2020; Priestley *et al.*, 2020a) and our limited theoretical understanding of how moist diabatic processes influence the evolution of storm tracks hinders our ability to identify causes of these biases. To alleviate these shortcomings, we quantify the role of diabatic processes in North Atlantic storm track, which encompasses both synoptic and lower-frequency variability. In addition, we assess the relative diabatic contributions of cyclones, fronts, and atmospheric rivers.

## 2 | DATA AND METHODS

We use the European Centre for Medium-Range Weather Forecasts (ECMWF) Reanalysis v5 (ERA5) data (Hersbach *et al.*, 2020) interpolated onto a $0.5° \times 0.5°$ longitude–latitude grid. We consider extended winters (November, December, January, February) from November 1979 to February 2020. We use three-hourly instantaneous fields of temperature ($T$), geopotential height ($z$), wind velocity ($u, v, w$), and total column water vapour (TCWV), as well as six-hourly accumulated precipitation (large-scale and convective) and temperature tendencies due to parametrisations (mttpm) centred on each three-hourly time step.

To compute the isentropic slope and its tendencies, we use $T$, $z$, $u$, $v$, $w$, and mttpm on 24 pressure levels (every 25 hPa between 1,000 hPa and 750 hPa, every 50 hPa thereafter up to 100 hPa). Temperature tendencies are only available on model levels, so we interpolated them to the same pressure levels.

### 2.1 | Isentropic slope framework

We use the isentropic slope framework (Papritz & Spengler, 2015) to calculate the diabatic and adiabatic tendencies in baroclinicity. Baroclinicity is measured as the slope $S \equiv |\nabla_\theta z|$ of isentropic surfaces, where the subscript indicates that the horizontal gradient is taken on an isentropic surface, with $z$ being the altitude of the surface. The Eulerian form of the slope tendency equation on pressure levels has three terms on the right-hand side that are responsible

for changes in the slope:

$$\left.\frac{\partial S}{\partial t}\right|_p = \underbrace{\frac{\nabla_\theta z}{S}\cdot\nabla_\theta w_{\mathrm{id}}}_{TILT} - \underbrace{\frac{\partial z}{\partial\theta}\frac{\nabla_\theta z}{S}\cdot\nabla_\theta\dot{\theta}}_{DIAB} - \underbrace{\frac{\partial S}{\partial\theta}\mathbf{v}\cdot\nabla\theta}_{ADV}. \quad (1)$$

The term labelled TILT is associated with the tilting of isentropic surfaces by the isentropic displacement vertical wind $w_{\mathrm{id}}$ (Hoskins *et al.*, 2003, eq. 8) and represents adiabatic contributions to changes in baroclinicity. The term DIAB describes the deformation of an isentropic surface due to diabatic heating. The TILT and DIAB terms generally exert opposing effects on the slope (Marcheggiani & Spengler, 2023; Papritz & Spengler, 2015). The term ADV, where $\mathbf{v} = (u, v, \omega)$ is the three-dimensional wind in pressure coordinates, represents the adiabatic advection of slope. The ADV term is typically much smaller than TILT and DIAB (Papritz & Spengler, 2015; Weijenborg & Spengler, 2020), especially above 800 hPa (not shown), so we neglect it in the present analysis.

Small-scale features (e.g., gravity waves) can give rise to an extremely steep slope and its tendencies, which are not relevant to study baroclinic development. Therefore, the data are first spatially filtered by spectral truncation to T84 to limit the effect of these small-scale structures. We focus on the free troposphere and consider vertical averages of slope, TILT, and DIAB between 750 hPa and 350 hPa (consistent with Marcheggiani & Spengler, 2023).

## 2.2 | Detection of weather features

For the detection and tracking of extratropical cyclones we implement a revised version of the algorithm developed by Murray and Simmonds (1991). Following Murray and Simmonds (1991), we first detect cyclones as maxima in the Laplacian of sea-level pressure (SLP) and then track cyclones using a Kalman filter to predict cyclone positions based on their previous movement. The resulting track is refined through a Kalman smoother, in which the best estimate of cyclone position and movement is updated using information from the respective following time steps. The use of a Kalman filter and smoother leads to more robust estimates of cyclone movement speed and direction. Finally, we retain cyclones that are tracked for at least 48 hr and travel more than 500 km between genesis and lysis.

When we mention cyclones, we refer to a certain area around their centre, similar to previous attribution studies (Catto & Dowdy, 2021; Konstali *et al.*, 2024). Whereas fronts and atmospheric rivers are often directly linked to a cyclone, they also extend quite far from their centre. Thus, any baroclinicity variability realised within fronts and atmospheric rivers is not necessarily directly attributed to a cyclone. A detailed description of the revised cyclone detection and tracking algorithm and specific choice of parameters can be found in Appendix A. The resulting dataset of cyclone detections and tracks for ERA5 is publicly available (Spensberger & Marcheggiani, 2024).

We identify fronts as coherent volumes with a thermodynamic gradient above a given threshold (Spensberger & Sprenger, 2018). Here, we use equivalent potential temperature at 700 hPa, 850 hPa, and 925 hPa and a gradient threshold of $|\nabla\theta_{\mathrm{E}}| > 5.3$ K/100 km. We then define a frontal area to be the intersection of this volume with the 850 hPa level, which is the level used by most front-detecting algorithms (Thomas & Schultz, 2019). As the front is originally detected as a volume, its intersection with the 850 hPa level will also contain information on the three-dimensionality of the front. For further details on the choice of the thermodynamic variable and gradient threshold, we refer the reader to Spensberger and Sprenger (2018).

The chosen front-detection algorithm does not capture any tilt of the frontal volume with height beyond 700 hPa, nor detect any upper level fronts that are detached from the surface. These undetected frontal features might also contribute to the total baroclinicity variability and explain part of the background variability. However, we restrict our attention to lower level fronts and their impact on free-tropospheric baroclinicity variability.

Finally, we follow Spensberger *et al.* (2025) and detect moisture transport axes (MTAs), defined as lines of well-defined maxima of vertically integrated water vapour transport. In the midlatitudes, MTAs correspond primarily to atmospheric rivers while also capturing the horizontal component of warm conveyor belts (Spensberger *et al.*, 2025). The ascending branch of warm conveyor belts, however, might not be detected as an MTA. Nonetheless, the ascending branch of warm conveyor belts is typically located in close proximity to a cyclone centre, thus also implicitly included in our analysis.

The implementations of all of the aforementioned detection and tracking algorithms are publicly available as part of dynlib (Spensberger, 2024).

## 2.3 | Contribution of weather features to the slope tendencies

We consider time series of area-mean diabatic (DIAB) and adiabatic (TILT) changes in baroclinicity over the Gulf Stream Extension region (80°–30°W, 30°–60°N, black box in Figure 1), which broadly corresponds to the North Atlantic storm track entrance. Consistent with Marcheggiani and Spengler (2023), we exclude land and ocean grid

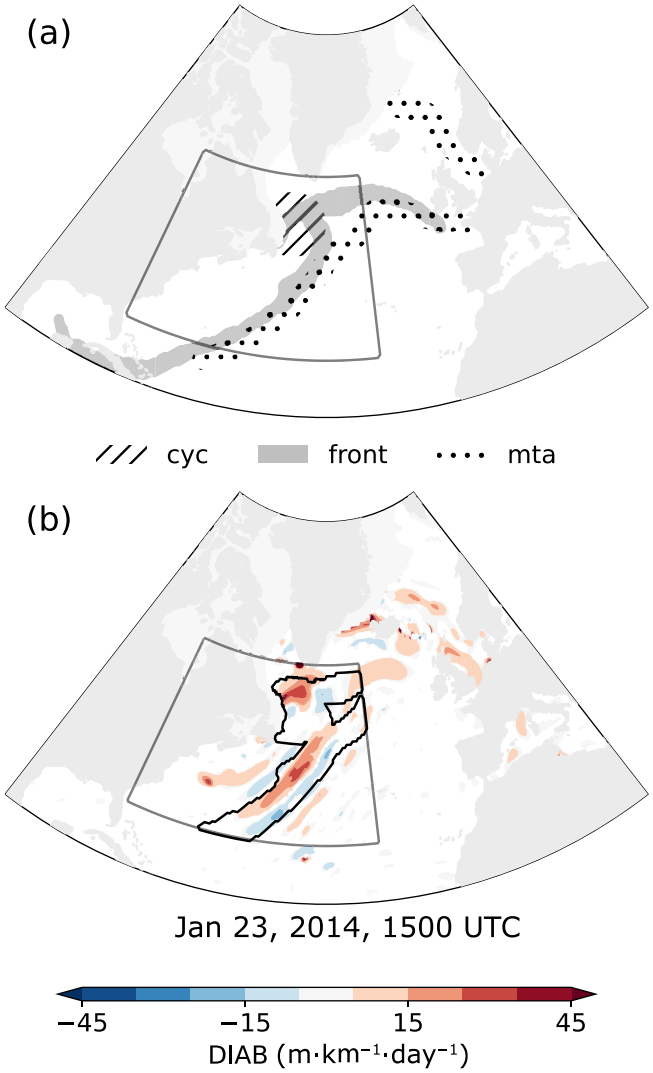


**FIGURE 1** Graphical example of spatial averaging conditioned on distance from weather features. (a) Location and corresponding mask $M$ used for spatial averaging of cyclones (hatches), fronts (darkest grey shading), and moisture transport axes (dots). (b) Effective area over which mean DIAB (shading) is calculated for the cyc + front + mta mean is indicated by a thick black contour ($M = 1$), whereas the grey box shows the total extent of the Gulf Stream Extension domain. Also marked are continents (medium-shaded grey) and ocean grid points where sea ice concentration is above 15% for more than 5% of the time (lightest grey shading), both excluded from spatial averaging. [Colour figure can be viewed at wileyonlinelibrary.com]

points where sea ice concentration is above 15% for more than 5% of the time (lightest grey shading in Figure 1) to limit the effects of inaccuracies in representing sea ice in reanalyses (Renfrew *et al.*, 2021).

We focus on the North Atlantic storm track entrance, because the signal is stronger and clearer there than in regions further downstream in the eastern North Atlantic and North Pacific (see Marcheggiani & Spengler, 2023), especially when considering spatial averages. We do not consider the entire North Atlantic basin either, as diabatic production and adiabatic depletion can occur simultaneously in the western and eastern sectors, which would hinder the detection of phasing between the two if we averaged DIAB and TILT over the entire North Atlantic.

We detect weather features as points (cyclones), areas (fronts), or lines (MTAs). To estimate the contribution from these features to the total diabatic and adiabatic changes in baroclinicity, we construct a spatial mask $M_f$ based on the distance from these features at each grid point:

$$M(\mathrm{lon}_i, \mathrm{lat}_i; t)_f = M_{i,f}(t) = \begin{cases} 1 & \text{if } d_{i,f}(t) \le D_f \\ 0 & \text{otherwise,} \end{cases} \tag{2}$$

where $d_{i,f}(t)$ represents the distance between a weather feature and a grid point with coordinates $(\mathrm{lon}_i, \mathrm{lat}_i)$ at time $t$, and $D_f$ is a distance threshold that characterises the size of the cyclone ($D_{\mathrm{cyc}}$), front ($D_{\mathrm{front}}$), or MTA ($D_{\mathrm{mta}}$) mask.

Any grid point with distance $D_f$ to one or more weather features is thus attributed to the corresponding weather features. Using the mask defined in Equation (2), for a variable $\chi$ (e.g., DIAB or TILT), we construct time series of feature-only area mean,

$$\chi_f(t) = \frac{\sum_i a_i\, M_{i,f}(t)\chi_i(t)}{\sum_i a_i M_{i,f}(t)}, \tag{3}$$

and no-feature area mean,

$$\chi_{\mathrm{nf}}(t) = \frac{\sum_i a_i(1 - M_{i,f}(t))\chi_i(t)}{\sum_i a_i(1 - M_{i,f}(t))}, \tag{4}$$

where the sums are over all grid points in the averaging box over the Gulf Stream Extension region, $a_i = a(\mathrm{lon}_i, \mathrm{lat}_i)$ is the area represented by each grid point, and $\chi_i(t) = \chi(\mathrm{lon}_i, \mathrm{lat}_i; t)$ is the value of variable $\chi$ at each grid point $i$ and time $t$.

At each time step, weather features occupy a fraction of the total area:

$$\alpha_f(t) = \frac{\sum_i a_i M_{i,f}(t)}{\sum_i a_i}. \tag{5}$$

The time series of the total area mean,

$$\chi_{\mathrm{tot}} = \frac{\sum_i a_i \chi_i(t)}{\sum_i a_i}, \tag{6}$$

is therefore the sum of the feature-focused component, Equation (3), and the background component, Equation

(4), weighted by the area fraction, Equation (5) they occupy:

$$\chi_{\text{tot}} = \alpha_f \chi_f + (1 - \alpha_f)\chi_{\text{nf}}. \tag{7}$$

We partition contributions from different features in a non-exclusive way, so grid points where two features overlap are assigned to both features. For example, if part of a front is located close enough to a cyclone centre, that part of the front will be included both in the cyclone ($\chi_{\text{cyc}}$) and in the front ($\chi_{\text{front}}$) area-mean time series. We present cumulative combinations of weather features starting from cyclones, then adding fronts, and finally atmospheric rivers, as the individual relative contribution from each of these features was also found to follow this order (see following section). In the Supporting Information we present different, non-exclusive combinations that provide further insight into the relative role that each feature plays.

Figure 1a shows features detected 23 January 2014, at 1500 UTC and the associated spatial masks: a cyclone is detected east of Newfoundland; fronts are detected around the cyclone's centre, extending both eastward and southwestward; an MTA is detected across the North Atlantic. Choosing $\chi = \text{DIAB}$, the time series for $\text{DIAB}_f$ corresponds to the area average of DIAB over the combined area of the three features outlined by the black contour in Figure 1b, whereas that for $\text{DIAB}_{\text{nf}}$ corresponds to the area mean outside of the features within the Gulf Stream Extension region. Numerically, $\alpha$ corresponds to the area within the black contour divided by total area within the Gulf Stream Extension region. In this example, we used $D_{\text{cyc}} = 600$ km, $D_{\text{front}} = 100$ km, and $D_{\text{mta}} = 200$ km, so cyclones, fronts, and MTAs combined occupy about 30% of the domain.

## 2.4 | Phase space analysis

Using the area-averaged fields of DIAB and TILT, we can construct a DIAB–TILT phase portrait by plotting the two time series against each other. We apply a Gaussian kernel with an averaging length scale set to 50% of the standard deviation of the given time series to filter out small-scale noise and define a streamfunction $\psi$ to visualise the non-divergent flow so that

$$\mathbf{F} = (\rho c_x, \rho c_y) = \left(-\frac{d\psi}{dy}, \frac{d\psi}{dx}\right), \tag{8}$$

where $\mathbf{F} = \rho\mathbf{c}$ is the mass flux, $\rho$ is the data density at each point in the phase space, and $\mathbf{c} = (c_x, c_y)$ represents the phase space velocity field. Specifically, $c_x$ and $c_y$ correspond to the kernel average of the time derivatives of area-mean DIAB and TILT respectively.

In the case of total variability, $\text{DIAB}_{\text{tot}}$ and $\text{TILT}_{\text{tot}}$ trace a clockwise circulation in the DIAB-TILT phase space, as indicated by the positive stream function (Figure 2). This circulation reflects the leading role of diabatic generation of baroclinicity over its adiabatic depletion, consistent with results by Marcheggiani and Spengler (2023).

We can estimate the typical period associated with oscillations in the phase portrait by first calculating the phase speed, $|\mathbf{c}|$, at each point in a closed contour of the stream function $\psi$, and then integrate this speed along the same contour. This provides a qualitative estimate of the average period of oscillations which we use primarily to assess the typical time scale associated with the circulation in the phase space. In particular, we obtain 2.6 days for the closed trajectory marked in red in Figure 2. For further details on the construction of phase portraits and related analysis, we refer the reader to Novak *et al.* (2017), Marcheggiani *et al.* (2022), as well as Marcheggiani and Spengler (2023).

The main difference between our study and Marcheggiani and Spengler (2023) lies in our use of a higher frequency time series (three-hourly versus six-hourly in Marcheggiani & Spengler, 2023). This change introduces a greater fraction of intra-day, high-frequency variability (for instance, the diurnal cycle) into the time series, which was implicitly filtered out in Marcheggiani and Spengler (2023). The additional high-frequency variability appears, however, to be coherent with lower frequency variability.

By low-pass time filtering $\text{DIAB}_{\text{tot}}$ and $\text{TILT}_{\text{tot}}$ (i.e., applying a 24-hr rolling average), we obtain a phase portrait (not shown) qualitatively similar to that in Figure 2, with typical oscillation periods of 5–6 days, in agreement with Marcheggiani and Spengler (2023). The complementary, high-frequency phase portrait (not shown), resulting from removing the 24-hr rolling average, is characterised by a similar clockwise circulation centred over the origin (DIAB = 0, TILT = 0). This suggests a link between high-frequency variability and smaller scale oscillations within the primary, lower frequency circulation. Considering the coherence between high- and low-frequency variability, shorter periods (2–3 days) for typical oscillations in the DIAB–TILT phase space simply result from the faster phase speeds observed in Figure 2 compared with Marcheggiani and Spengler (2023) (4–6 days). To minimise data manipulation, we nevertheless retain the full time series throughout this study without introducing any time filtering.

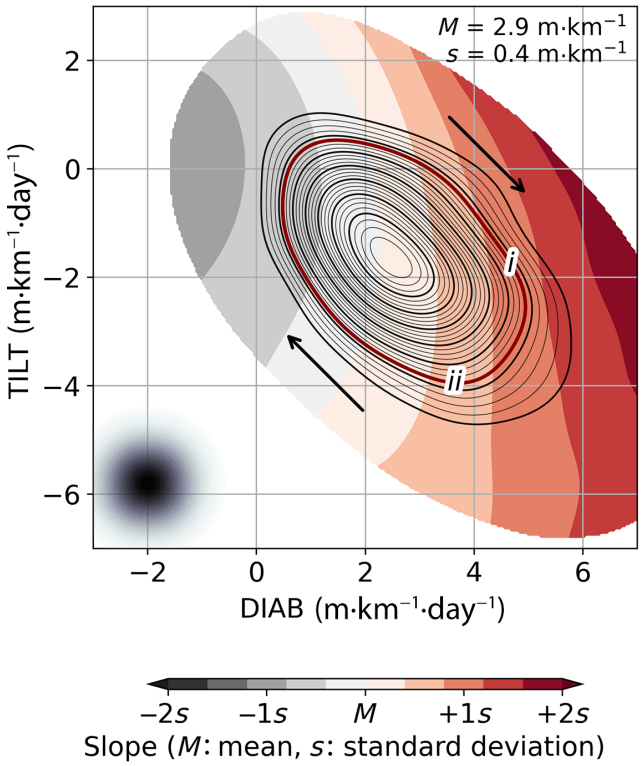


**FIGURE 2** Phase portrait of DIAB ($x$ coordinate) and TILT ($y$ coordinate) spatially averaged over the Gulf Stream Extension region. Shading represents the kernel-averaged mean slope, offset and scaled according to the mean and standard deviations of the slope time series respectively, annotated in the upper right corner. Contours represent the stream function associated with the kernel-averaged phase-space circulation. Arrows indicate the clockwise direction of the circulation. Points where data are scarce (less than 0.5% of maximum data density) are blanked out. The size of the Gaussian filter used to construct the phase portrait is indicated by the black-shaded dot in the lower left corner. Lower case Roman numerals (i, ii) indicate the two different points along a chosen closed contour of the stream function (thick red) in the phase space where the kernel composites are evaluated (Figures 6 and 7). [Colour figure can be viewed at wileyonlinelibrary.com]

## 3 | QUANTIFYING FEATURE CONTRIBUTION TO TOTAL VARIABILITY

The case in Figure 1 suggests that a large portion of the total spatial variability of DIAB within the Gulf Stream Extension is co-located with cyclones, fronts, and MTAs. To quantify how much of the total variability is associated with weather features, we consider the fraction $R_f$ of total variance explained by features, measured as the covariance of $\chi_{\text{tot}}$ and $\chi_f$ divided by the variance of $\chi_{\text{tot}}$:

$$R_f = \frac{\text{Cov}(\chi_{\text{tot}}, \chi_f)}{\text{Var}(\chi_{\text{tot}})}. \quad (9)$$

Given that larger time-mean feature area fractions $\overline{\alpha_f}$ correspond with larger fractions of total variance explained $R_f$, we need to quantify how much of the increase in $R$ with $\overline{\alpha_f}$ is due to inflating the area attributed to features versus how much is due to changes of the variance within the features themselves.

We explore this relation by modulating the areal extent attributed to features by linearly increasing the distance threshold $D_f$, Equation (2) (and implicitly in Equations 3–5). In particular, we maintain the same proportion between $D_{\text{cyc}}$, $D_{\text{front}}$, and $D_{\text{mta}}$, such that $D_{\text{cyc}} = 3 \times D_{\text{mta}} = 6 \times D_{\text{front}}$, and thus consider the following:

- $D_{\text{cyc}}$ from 300 km to 2,400 km with a step of 300 km;
- $D_{\text{front}}$ from 50 km to 400 km with a step of 50 km;
- $D_{\text{mta}}$ from 100 km to 800 km with a step of 100 km.

We then plot the fraction of DIAB and TILT variance explained by features resulting from the different $D_f$ used against their mean fractional areal extent (Figure 3). We perform this analysis for cyclones only (cyc, Figure 3a), cyclones and fronts (cyc + front, Figure 3b), and cyclones, fronts, and MTAs (cyc + front + mta, Figure 3c). We consider these specific, cumulative combinations because they provide the clearest results, especially when looking at phase portraits which are presented in the following sections.

Regardless of the choice for $D$, the fraction of total variance explained by features is larger than the mean area fraction occupied, given that all scatter points are above the diagonal, where $R_f = \overline{\alpha_f}$ (Figure 3). The diagonal represents the trend that would be expected if DIAB/TILT variability was randomly distributed across the averaging box. In that case, an increase in variance explained would scale linearly with the area fraction over which the variance is calculated. Below this line, more variance is realised outside of the reference area (e.g., cyclone mask) than inside.

For low distance thresholds (darker blue markers), features capture a fraction of total variability that is between two and three times larger than their mean area fraction, highlighting that peaks in DIAB and TILT mostly occur near weather features. Larger distance thresholds (brightest yellow markers) are associated with largest mean area fractions and the fraction of variance explained by features approaches unity. Past a certain size, the increase in variance explained with increasing area fraction weakens, as we include exceedingly more non-feature-related background variability.

Given the same mean area fraction $\overline{\alpha_f}$, features explain less of the total variance for TILT than for DIAB. For

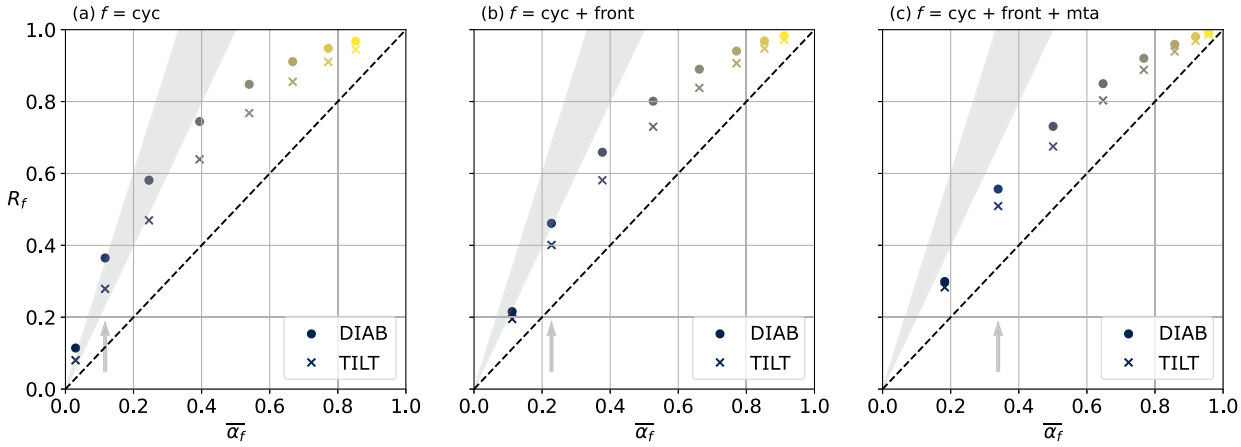


**FIGURE 3** Fraction $R_f$, Equation (9), of DIAB (dots) and TILT (crosses) for $f$ indicating (a) cyclones alone, (b) cyclones and fronts, and (c) cyclones, fronts, and moisture transport axes plotted against the mean area fraction occupied by the different feature combinations $\overline{\alpha_f}$. Markers are colour coded according to distance threshold $D_f$ used, Equation (2), from dark blue ($D_{\text{cyc}} = 100$ km) to lighter yellow ($D_{\text{cyc}} = 800$ km), every 100 km. Dashed line indicates where $R_f = \overline{\alpha_f}$, whereas grey shaded area highlights sector where ratio between $R_f$ and mean $\overline{\alpha_f}$ is in the range 2:1–3:1. Arrows indicates points corresponding to distance threshold used in the rest of this study. [Colour figure can be viewed at wileyonlinelibrary.com]

example, cyclones with $D_{\text{cyc}} = 600$ km (Figure 3a, highlighted by grey arrow) occupy on average 10% of the domain and explain almost 40% of the total variance in DIAB ($R^{\text{DIAB}}_{\text{cyc}} = 0.37$), but less than 30% of the total variance in TILT ($R^{\text{TILT}}_{\text{cyc}} = 0.28$). This difference is likely due to the larger amount of noise that characterises TILT (Papritz & Spengler, 2015), with more variance also outside of the features.

The difference in $R_f$ for DIAB and TILT becomes less pronounced when considering the combination of all features (cyclone + front + mta, Figure 3c). Larger values of area fraction covered when all features are considered partly explains the reduced difference in $R_f$, as most of the variability in both DIAB and TILT is likely to occur within the feature mask. However, this difference does not depend exclusively on $\alpha_f$, as we still observe smaller differences for similar values of $\alpha_f$. For example, for cyclones ($f$ = cyc, Figure 3a) $\alpha_f = 0.4$ and $\Delta R_f \equiv R^{\text{DIAB}}_f - R^{\text{TILT}}_f \approx 0.1$, whereas for all features ($f$ = cyc + front + mta, Figure 3c) $\Delta R_f = 0.05$–$0.06$ for $\alpha_f = 0.3$–$0.5$.

Moreover, the difference $\Delta R_f$ changes sign when considering fronts and MTAs alone as well as their combination (Supporting Information Figure S1a-c). This is especially true around MTAs, explaining a smaller fraction of the total variance in DIAB than in TILT, indicating that DIAB is not primarily associated with MTAs alone. This is consistent with Konstali *et al.* (2024), who demonstrated that the higher concentration of moisture around MTAs does not necessarily lead to precipitation (and thus latent heating), as lift is also needed to create precipitation.

For the remaining analyses we use the following distance thresholds:

- $D_{\text{cyc}} = 600$ km from cyclone centres;
- $D_{\text{front}} = 100$ km from fronts[1];
- $D_{\text{mta}} = 200$ km from MTAs.

These distance thresholds are highlighted by arrows in Figure 3. Using a radius of 600 km around cyclones yields a typical area fraction covered by cyclones of $\overline{\alpha}_{\text{cyc}} \approx 0.12$, which is comparable to the value obtained using alternative detection methods, such as the algorithm by Wernli and Schwierz (2006), which yields around 0.10.

## 4 | FEATURE-BASED PHASE PORTRAITS

Even though weather features explain 30–60% of the total variability while only occupying between 10 and 30% of the total domain (Figure 3), these statistics do not indicate to what extent the total variability around weather features is coherent with the total variability. Hence, we construct phase portraits based on time series of feature-based area means $\chi_{\text{f}}$ , Equation (3) (Figure 4a–c).

The clockwise direction of the phase-space circulation for feature-based variability is coherent with the total variability. However, the amplitudes of the oscillations of both TILT and DIAB are significantly larger around features than the total variability phase portrait is (compare

Figure 4a–c with Figure 2, whose extent is also shown in Figure 4). For cyclones (Figure 4a), the amplitude of the phase-space circulation is up to $\pm 20\ \mathrm{m \cdot km^{-1} \cdot day^{-1}}$ compared with $\pm 5\ \mathrm{m \cdot km^{-1} \cdot day^{-1}}$ for the total time series (Figure 2). If we include fronts, we obtain slightly weaker oscillations than with cyclones alone, though still reaching peaks of up to $15\ \mathrm{m \cdot km^{-1} \cdot day^{-1}}$ (Figure 4b), significantly larger than the total time series (Figure 2). Finally, the inclusion of MTAs further weakens the amplitude of oscillations to $\pm 12\ \mathrm{m \cdot km^{-1} \cdot day^{-1}}$ (Figure 4c), though still larger than the total (Figure 2).

For all combinations of weather features, as well as the background and total, the steepest slope (1–1.5 standard deviations above the time mean) also coincides with the strongest DIAB, indicating that stronger diabatic generation of slope is generally associated with steeper slope. However, we find stronger area-mean slope in correspondence with cyclones and, to a lesser extent, with fronts and MTAs than with the total area-mean. In particular, we find area-mean slopes around cyclones and fronts of $3.3–3.7\ \mathrm{m \cdot km^{-1}}$ (Figure 4a,b, upper right corner) whereas for the total it is $2.9\ \mathrm{m \cdot km^{-1}}$ (Figure 2). We also notice significantly larger variability in the time series for cyclones and fronts, with standard deviations around $0.7–1.3\ \mathrm{m \cdot km^{-1}}$, two to three times as large as that of the total time series ($0.4\ \mathrm{m \cdot km^{-1}}$, Figure 2). When we include MTAs, thus considering the combination of all weather features, the resulting area-mean slope ($3.0\ \mathrm{m \cdot km^{-1}}$, Figure 4c) is close to that for the total, though there is still slightly more variability (standard deviation of $0.6\ \mathrm{m\ km^{-1}}$, Figure 4c).

The relationship between DIAB and TILT along fronts alone is qualitatively similar (Supporting Information Figure S2a), whereas it becomes less clear around MTAs (Supporting Information Figure S2b), where small-scale, noisy features dominate the phase-space circulation, suggesting the DIAB–TILT relationship is not as well defined

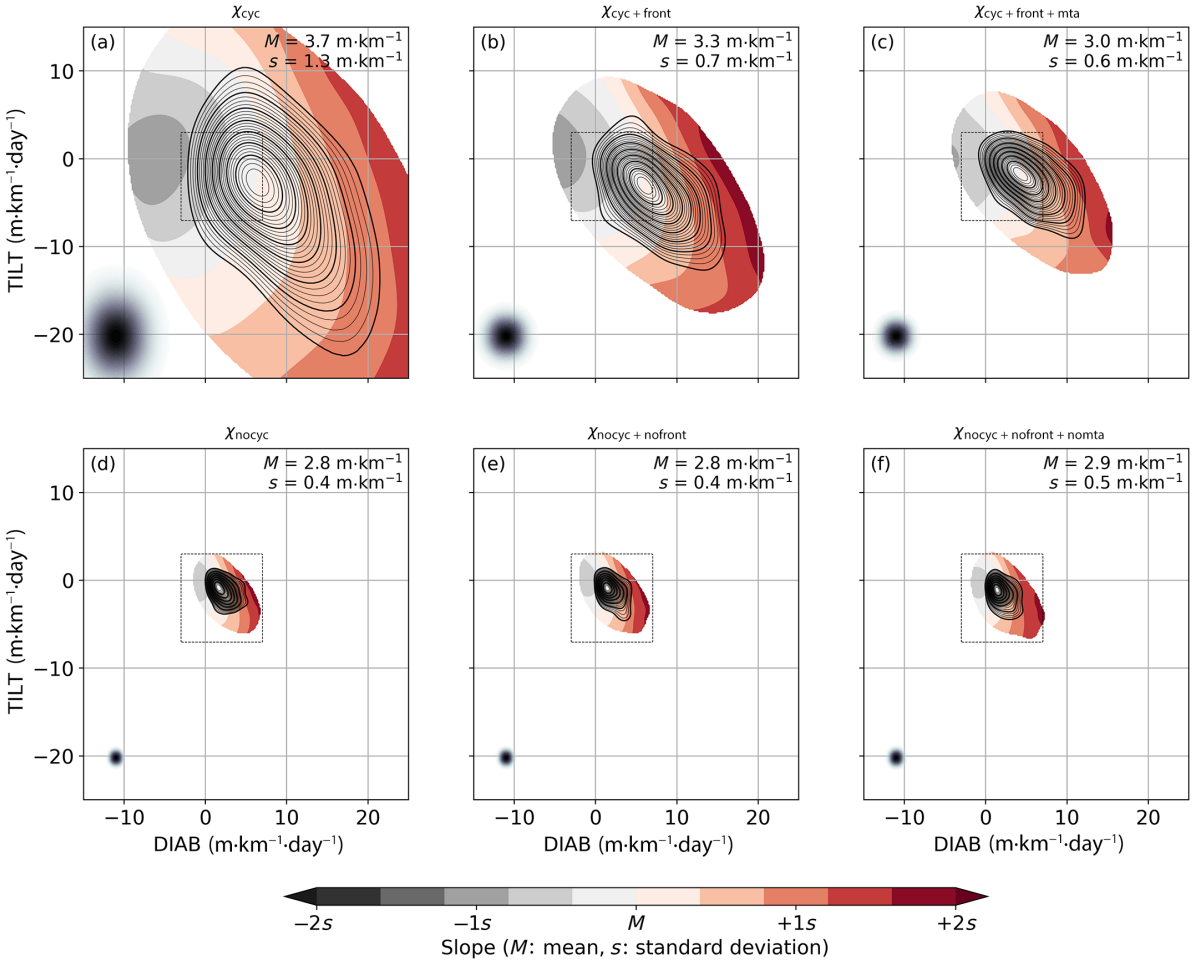


**FIGURE 4** Phase portraits constructed as in Figure 2, here using time series for the spatial averages focused on (a) cyclones, (b) cyclones and fronts, and (c) cyclones, fronts, and moisture transport axes (MTAs). (d)–(f) Spatial averages excluding (d) cyclones, (e) cyclones and fronts, and (f) cyclones, fronts, and MTAs. Dashed box represents size of domain showed in Figure 2. [Colour figure can be viewed at wileyonlinelibrary.com]

around MTAs. This is consistent with Konstali *et al.* (2024), who argue that MTAs only indicate the presence of moisture but are not necessarily directly related to precipitation, and thereby diabatic heating.

For the no-feature time series of background variability $\chi_{\mathrm{nf}}$, Equation (4), the resulting phase portraits (Figure 4d–f) are also coherent with the total variability (same shape and clockwise direction of the circulation). However, oscillations are substantially weaker than their feature-based counterparts (compare Figure 4d–f and Figure 4a–c, showing background and feature-focused phase portraits respectively). The extent of the circulation and data density in the background phase portraits (Figure 4d–f) are, however, comparable to the total time series (Figure 2, note different axes boundaries). We also find that the typical area-mean slope in the background variability (2.8–2.9 $\mathrm{m}\cdot\mathrm{km}^{-1}$, Figure 4d–f) is similar to the total (2.9 $\mathrm{m}\cdot\mathrm{km}^{-1}$, Figure 2), with the same levels of variability around the mean value (standard deviations around 0.4–0.5 $\mathrm{m}\cdot\mathrm{km}^{-1}$). This suggests that steeper slope is usually found around weather features rather than in the background.

### 4.1 | Phase portraits of partitioned variability

Despite the large amplitudes in the oscillations in the feature-based phase space circulation (Figure 4a–c), amplitudes of the oscillation in the total variability phase space are more comparable to those in the background phase space (compare Figure 2 with Figure 4d–f). To further clarify the relative contribution of the feature-based and background variability, we quantify the contribution of feature-based and background to the total variability by separately considering the two terms on the right-hand side of Equation (7). Thus, the superposition of the feature-based circulations (Figure 5a–c) with the corresponding background circulations (Figure 5d–f) yields the circulation for the total time series (Figure 1). Here, the amplitudes of the oscillations can be interpreted as the relative contribution to the total phase-space circulation.

The amplitudes of the oscillations have now a comparable magnitude, whereas the clockwise direction of the phase-space circulation remains unchanged. For cyclones, we observe amplitudes up to $\pm 3\ \mathrm{m}\cdot\mathrm{km}^{-1}\cdot\mathrm{day}^{-1}$ (Figure 5a) and slightly larger outside cyclones (up to $\pm 4\ \mathrm{m}\cdot\mathrm{km}^{-1}\cdot\mathrm{day}^{-1}$, Figure 5d). The combination of cyclones and fronts compares similarly (Figure 5b,e), whereas when we include MTAs the magnitude of oscillations (Figure 5c) is qualitatively identical to those for the background (Figure 5f).

The total circulation (Figure 2) is roughly the sum of the feature-based and background circulations (each column of Figure 5). Hence, weather features and background contribute equally and coherently to the total variability, though weather features extend over a much more limited area compared with the background.

The contribution from alternative combinations of these three weather features is generally consistent with the results reported herein. Fronts and MTAs contribute a sizeable fraction of the total variability despite the low area-fraction they occupy (curve above the $R_f = \overline{\alpha_f}$ line in Supporting Information Figure S1a–c), both individually (Supporting Information Figure S1a,b) and in combination (Supporting Information Figure S1c). However, phase portraits of partitioned variability (Supporting Information Figure S3a-c) are visibly more noisy than that for cyclone combinations (Figure 5b,c and Supporting Information Figure S3d), indicating that their contribution to total variability is less coherent. In particular, the contribution from MTAs is least coherent, regardless of whether their spatial extent is accounted for (Supporting Information Figure S3b) or not (Supporting Information Figure S2b).

## 5 | SYNOPTIC EVOLUTION

To better understand the circulation in the phase space, we compile composites of atmospheric conditions for two typical positions in the DIAB–TILT phase space: (i) maximum DIAB and (ii) maximum TILT (Figures 2 and 5c,f). Stages (i) and (ii) respectively correspond to the second and third stages described in Marcheggiani and Spengler (2023).

Considering the total variability, stage (i) is characterised by strong DIAB over large parts of the Gulf Stream Extension (Figure 6a) whereas TILT remains relatively weak (Figure 6b). Peaks of DIAB coincide with strong precipitation south and east of a relatively dry air mass (15–40% drier than climatology). This dry air mass appears to broadly correspond with the cold sector associated with the deepening cyclonic anomaly centred east of Newfoundland (negative geopotential), which presents a clear baroclinic structure with a westward tilt with height (Figure 6b). Composites of cyclone track density (not shown) also indicate the relatively higher occurrence of cyclones in correspondence with the negative surface geopotential anomaly.

The feature-based composites are nearly identical to the total composites for stage (i). The geopotential anomalies for the features-based composite match the anomalies in the total composite both in terms of space and magnitude, with only slightly weaker negative anomalies (lowest

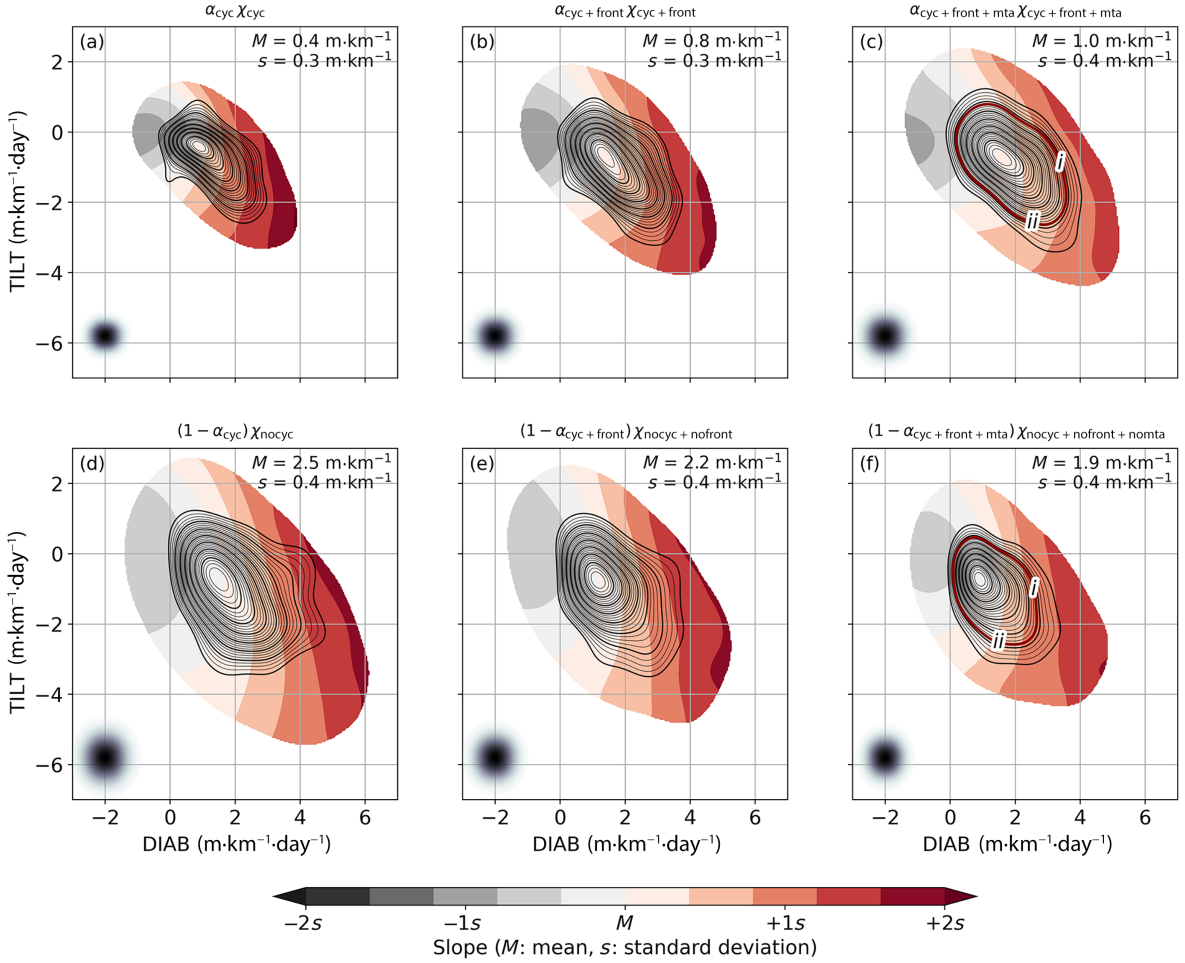


**FIGURE 5** As in Figure 4, but for the product of area fraction $\alpha$ and the area average focused on features. [Colour figure can be viewed at wileyonlinelibrary.com]

contour at −14 dam in Figure 6d compared with −18 dam in Figure 6b). The distribution and intensity of DIAB and TILT also closely resemble each other, with the largest area-mean DIAB concurring with the presence of weather features (Figure 6a–d). The same is true for total precipitation, coinciding with the strongest DIAB, and for TCWV, highlighting the dry air mass over the northeastern American continent.

In stage (ii), DIAB has partially subsided (Figure 7b) whereas TILT attains peak strength (Figure 7a), which implies that the atmospheric flow is highly conducive to baroclinic conversion. However, because the mean isentropic slope is already past its maximum value, the structure of the flow becomes less baroclinic and more barotropic (see geopotential in Figure 7b) as the slope is adiabatically flattened.

At the point of maximum baroclinic conversion, weather systems tend to be past their maximum intensification and have travelled further downstream towards the eastern North Atlantic and Europe. In contrast to the upstream region, where cyclone tracks are more tightly distributed south of Greenland, tracks become more dispersed as cyclones progress across the Atlantic (see Supporting Information Figure S4a,c vs. Supporting Information Figure S4b,f). Thus, composites during this later stage are based on a broader set of more widely scattered systems, which reduces the clarity of the averaged fields. Nevertheless, key features such as a predominantly barotropic structure and regions of intensified synoptic activity remain evident. In particular, the geopotential composite shows an extended trough off the east coast of North America, accompanied by an increase in cyclone track density in this area (Supporting Information Figure S4a,c), compared with the earlier stage (Figure 4b,d). This suggests the likely occurrence of secondary cyclogenesis in that region.

Additionally, we observe an overall increase in moisture content within the Gulf Stream Extension, with mean TCWV rising from 12.7 kg · m$^{-2}$ in stage (i) to approximately 13.2 kg · m$^{-2}$ in stage (ii), whereas precipitation is

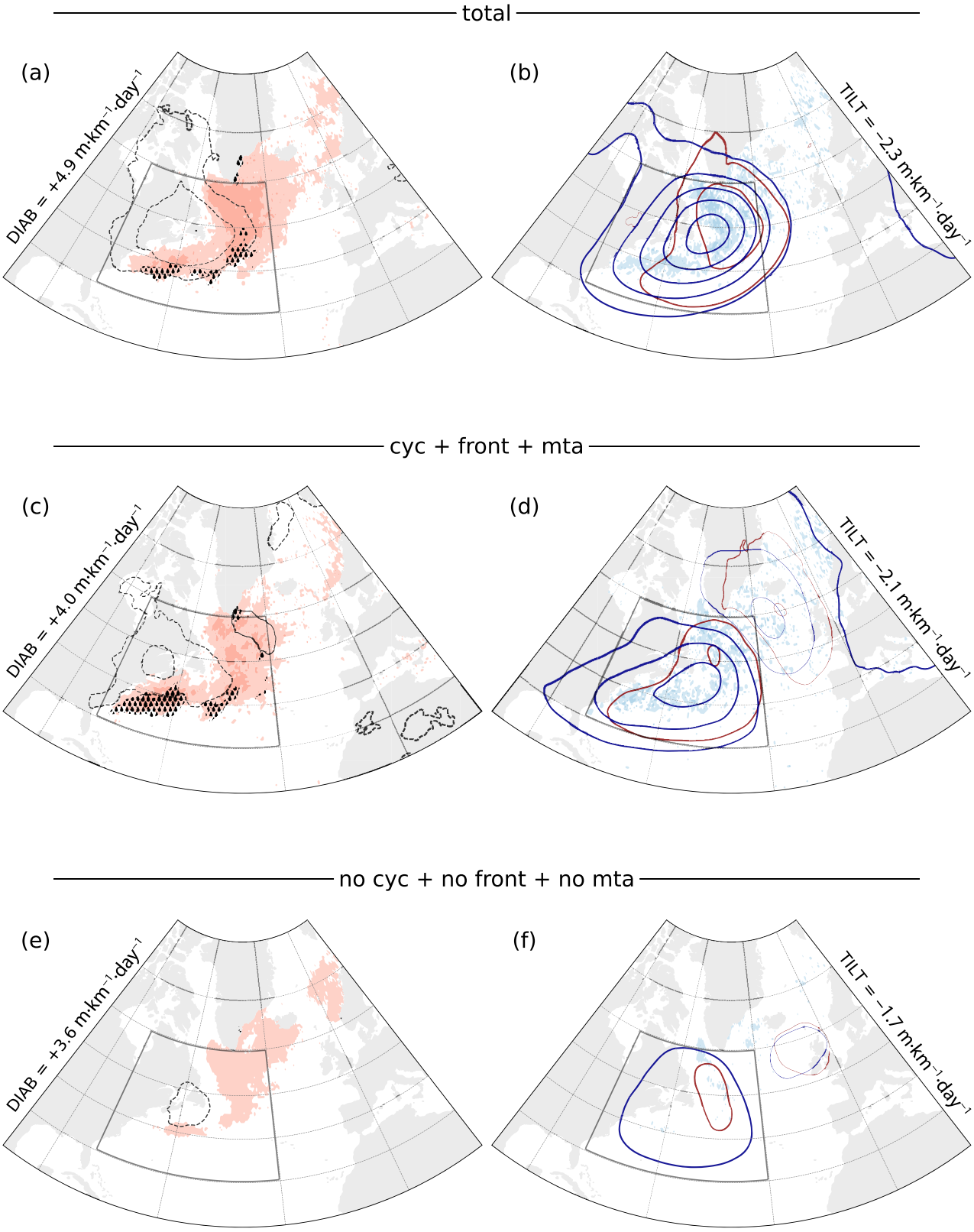


**FIGURE 6** Phase composites for stage (i) for (a, b) total, (c, d) feature-based, and (e, f) background phase portraits (Figures 2 and 4c,f). (a, c, e) DIAB (red shading, lighter between 4 and 8 m · km$^{-1}$ · day$^{-1}$, darker above), ratio of TCWV to climatology (black contours, at ±15% and ±30%, negative values dashed), and total precipitation (stippling, above 10 mm · day$^{-1}$). (b, d, f) TILT (blue shading, lighter between −4 to −8 m · km$^{-1}$ · day$^{-1}$, darker below), Z1000 and Z500 anomalies from climatology (red and blue respectively; every 4 dam, omitting 0 dam; thicker contours denote negative values). Area-mean values of DIAB and TILT for this stage are indicated outside of each panel to the left and right respectively. [Colour figure can be viewed at wileyonlinelibrary.com]

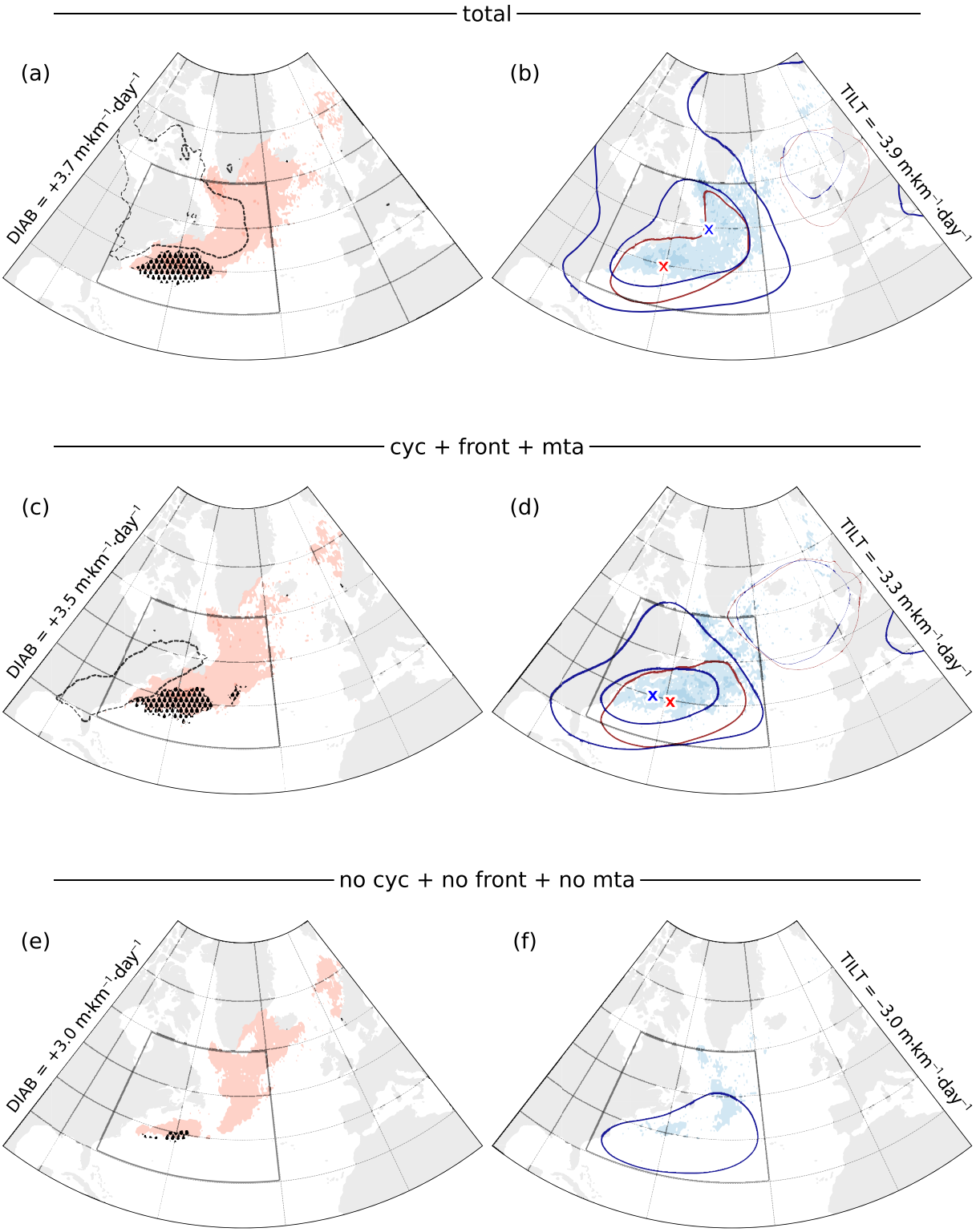


**FIGURE 7** Same as Figure 6 but for stage (ii). Crosses in (b) and (d) mark the location of the minima in Z1000 (red) and Z500 (blue) anomalies. [Colour figure can be viewed at wileyonlinelibrary.com]

concentrated over the southwestern edge of the geopotential trough (compare Figure 7a,b). Despite the increase in TCWV, the region remains about 15% drier than the climatological average, as shown by the negative anomalies in Figure 7a).

DIAB, TILT, and precipitation for the feature-based composites in stage (ii) are still virtually identical to the total composites (compare Figure 7a,b and Figure 7c,d). The moisture distribution, on the other hand, is slightly more prominent in the total composite (Figure 7a), with

the dry signal over the Gulf Stream Extension being absent in the feature-focused composite (Figure 7c). The feature-based geopotential composite qualitatively resembles the total composite, with slightly stronger anomalies at the surface (minimum in Z1000 anomaly of −5.7 dam in Figure 7d compared with −4.8 dam in Figure 7b, marked by red crosses) and similar though more spatially constrained higher up in the free troposphere (minima in Z500 anomaly of −9.3 dam and −9.1 dam in Figure 7b,d respectively, marked by blue crosses), and highlights the southwestern section of the cyclonic circulation as well as the main anticyclonic anomaly further downstream in the eastern North Atlantic. As area-mean TILT attains its maximum strength ($-3.9\ \mathrm{m}\cdot\mathrm{km}^{-1}\cdot\mathrm{day}^{-1}$ and $-3.2\ \mathrm{m}\cdot\mathrm{km}^{-1}\cdot\mathrm{day}^{-1}$ for the total and feature-based respectively; Figure 7b,d), the signature from weather features becomes weaker, both in the total and in the feature-focused composites, suggesting that the adiabatic depletion of baroclinicity is not tightly linked to weather features.

Composites based on background variability display notably weaker anomalies than total and feature-based composites do (Figures 6c–f and 7c–f), despite retaining some similarity in their spatial structure. The gradient in the spatial distribution of moisture is also considerably weaker, with a higher moisture content in both stages ($13.7–14\ \mathrm{kg}\cdot\mathrm{m}^{-2}$) than in the total and feature-based composites ($12.7–13.2\ \mathrm{kg}\cdot\mathrm{m}^{-2}$) and no clear signature of the cold and dry air mass that characterises the first stage (Figure 6a,c). Hence, our analysis implies that the physical mechanisms driving the storm track evolution are primarily linked to synoptic features, whereas there is no clear synoptic mechanism driving background variability.

Phase portraits based on $\chi_{\mathrm{front}}$ (Supporting Information Figure S2a), $\chi_{\mathrm{mta}}$ (Supporting Information Figure S2b), and their combination (Supporting Information Figure S2c) suggest variability within fronts and MTAs is equally large as around cyclones alone (Figure 4a). However, when scaled by their areal extent, variability within fronts (Supporting Information Figure S3a) and MTAs (Supporting Information Figure S3b) is visibly noisier and less coherent with the total variability (Figure 2). The secondary, anticlockwise circulation suggests that there is no clear phasing between DIAB and TILT along MTAs. As TILT increases, DIAB can be weak or strong. In statistical terms, this circulation is not an artefact of kernel smoothing and represents a real mean behaviour of the DIAB-TILT relationship within MTAs. However, its physical significance is questionable.

Composites along the primary, clockwise, and secondary, anticlockwise, circulation cells (not shown) are noisy and do not reveal any clear synoptic evolution, which is indicative of the lack of any clear physical meaning behind these secondary cells. This is similar to what is found in composites based on background variability, which show clear circulation patterns in the phase portrait (Figure 5f) but no clear physical mechanism associated with it (Figures 5e,f and 6e,f).

## 6 | CONCLUSIONS

Moist dynamic processes exert a crucial influence on the midlatitude atmospheric circulation, contributing to the diabatic maintenance of baroclinicity within storm tracks. Given that moist dynamic processes are primarily associated with synoptic weather features, such as extratropical cyclones, fronts, and atmospheric rivers (here MTAs), we quantified the contribution of these features to the total baroclinicity variability in the North Atlantic storm track entrance. We find that most of the diabatic generation of baroclinicity (DIAB) and its adiabatic depletion (TILT) occur within cyclones, fronts, and MTAs rather than in the surrounding background environment. These three weather features combined explain up to 60–65% of the total time variance of DIAB and TILT in the Gulf Stream Extension region while, on average, covering only 30% of the domain.

Among all weather features, cyclones constitute the largest individual contribution, explaining almost half the total DIAB and TILT time variance in the storm track despite only covering an average of 10–20% of the domain. Fronts are the second largest individual contributor to the total variability, but the contribution from MTAs is less clear. Despite explaining a relatively large fraction of the total variance, the phase-space circulation associated with MTAs is the most noisy and incoherent, suggesting that MTAs alone are not an active dynamic contributor to storm track variability. This fact is congruent with MTAs alone not contributing significantly to precipitation, and thus diabatic heating, in the storm track regions (Konstali *et al.*, 2024).

Background variability outside of features also contributes to the total variability, with DIAB leading in time over TILT. However, though the contribution of the background is coherent with the total variability, its relative contribution to the total variability is small compared with its area fraction. Overall, the background explains less than 40% of the total variance in the storm track's baroclinicity despite extending over 70% of the domain.

Assessing the typical synoptic evolution using composites along the phase-space circulation, we find that the strongest area-mean DIAB (i) concurs with a strong gradient in the distribution of moisture, which is primarily associated with a dry anomaly co-located with the cold sector of a cyclone. Subsequently, at the time of strongest TILT (ii), composites highlight a moisture distribution

closer to climatology while indicating upstream cyclogenesis, though the signal is rather weak. The synoptic patterns emerging from feature-focused phase-space composites strongly resemble the composites for the total variability, both in terms of spatial distribution and intensity. Synoptic composites for the background, on the other hand, show much weaker signals than both total and feature-based composites do, indicating that there is no coherent synoptic evolution associated with background variability.

Overall, our results confirm the crucial role of synoptic weather features, such as cyclones, fronts, and MTAs, for the total baroclinicity variability in the North Atlantic storm track. The largest diabatic production of baroclinicity is tightly linked to cyclones, both individually and in combination with fronts, consistent with the hypothesis proposed by Marcheggiani and Spengler (2023), whereas its adiabatic depletion occurs irrespective of the presence of these weather features. Our results are congruent with previous publications emphasising the primary role of the aforementioned weather features on the climatological distribution of precipitation (Catto & Pfahl, 2013; Konstali *et al.*, 2024; Pfahl & Wernli, 2012) as well as the net meridional heat transport (Messori *et al.*, 2017; Messori & Czaja, 2013, 2015). Diabatic processes linked to these synoptic features are thus central to the evolution of storm tracks and thus need to be adequately represented to correctly represent baroclinicity variability within midlatitude storm tracks.

## ACKNOWLEDGEMENTS

We would like to thank the three anonymous reviewers for the useful comments that helped improve this article. We also wish to thank the ECMWF for making their reanalysis data freely available. AM, CS, and TS acknowledge the support from the Norwegian Research Council (Norsk Forskningsråd, NFR) via the BALMCAST project (NFR Project 324081). We also acknowledge the Bjerknes Centre for Climate Research for supporting HD's research visit to Bergen via the Bjerknes Visiting Fellow programme.

## DATA AVAILABILITY STATEMENT

The Python library dynlib is freely available at https://doi.org/10.5281/zenodo.10471187 (Spensberger, 2024). Data from ERA5 (Hersbach *et al.*, 2020) are available at https://doi.org/10.24381/cds.adbb2d47. Cyclone tracks based on ERA5 data are openly available at https://doi.org/10.11582/2024.00023.

## ENDNOTE

[1]Fronts are already identified as areas; however, we use a non-zero threshold to make the mask more coherent compared with the original based on $\theta_E$ gradient threshold.

## ORCID

*Andrea Marcheggiani* https://orcid.org/0000-0002-3571-608X
*Helen Dacre* https://orcid.org/0000-0003-4328-9126
*Clemens Spensberger* https://orcid.org/0000-0002-9649-6957
*Thomas Spengler* https://orcid.org/0000-0002-1747-6385

## REFERENCES

Auestad, H., Spensberger, C., Marcheggiani, A., Ceppi, P., Spengler, T. & Woollings, T. (2024) Spatio-temporal filtering of jets obscures the reinforcement of baroclinicity by latent heating. *EGUsphere*, 1–19, 2024.

Bjerknes, J. (1922) Life cycle of cyclones and the polar front theory of atmospheric circulation. *Geofysiske Publikasjoner*, 3, 1–18.

Catto, J.L. & Dowdy, A. (2021) Understanding compound hazards from a weather system perspective. *Weather and Climate Extremes*, 32, 100–313.

Catto, J.L. & Pfahl, S. (2013) The importance of fronts for extreme precipitation. *Journal of Geophysical Research: Atmospheres*, 118, 10–791.

Chaboureau, J.-P. & Thorpe, A.J. (1999) Frontogenesis and the development of secondary wave cyclones in FASTEX. *Quarterly Journal of the Royal Meteorological Society*, 125, 925–940.

Chang, E.K. (2009) Diabatic and orographic forcing of northern winter stationary waves and storm tracks. *Journal of Climate*, 22, 670–688.

Fuchs, D., Sherwood, S.C., Waugh, D., Dixit, V., England, M.H., Hwong, Y.-L. et al. (2023) Midlatitude jet position spread linked to atmospheric convective types. *Journal of Climate*, 36, 1247–1265.

Garfinkel, C.I., Keller, B., Lachmy, O., White, I., Gerber, E.P., Jucker, M. et al. (2024) Impact of parameterized convection on the storm track and near-surface jet response to global warming: implications for mechanisms of the future poleward shift. *Journal of Climate*, 37, 2541–2564.

Harvey, B., Cook, P., Shaffrey, L. & Schiemann, R. (2020) The response of the northern hemisphere storm tracks and jet streams to climate change in the CMIP3, CMIP5, and CMIP6 climate models. *Journal of Geophysical Research: Atmospheres*, 125, e2020JD032701.

Hersbach, H., Bell, B., Berrisford, P., Hirahara, S., Horányi, A., Muñoz-Sabater, J. et al. (2020) The ERA5 global reanalysis. *Quarterly Journal of the Royal Meteorological Society*, 146, 1999–2049.

Hoskins, B.J. & Valdes, P.J. (1990) On the existence of storm-tracks. *Journal of the Atmospheric Sciences*, 47, 1854–1864.

Hoskins, B., Pedder, M. & Jones, D.W. (2003) The omega equation and potential vorticity. *Quarterly Journal of the Royal Meteorological Society: A Journal of the Atmospheric Sciences, Applied Meteorology and Physical Oceanography*, 129, 3277–3303.

Hotta, D. & Nakamura, H. (2011) On the significance of the sensible heat supply from the ocean in the maintenance of the mean baroclinicity along storm tracks. *Journal of Climate*, 24, 3377–3401.

Konstali, K., Spensberger, C., Spengler, T. & Sorteberg, A. (2024) Global attribution of precipitation to weather features. *Journal of Climate*, 37, 1181–1196.

Marcheggiani, A. & Spengler, T. (2023) Diabatic effects on the evolution of storm tracks. *Weather and Climate Dynamics*, 4, 927–942.
Marcheggiani, A., Ambaum, M.H. & Messori, G. (2022) The life cycle of meridional heat flux peaks. *Quarterly Journal of the Royal Meteorological Society*, 148, 1113–1126.
Messori, G. & Czaja, A. (2013) On the sporadic nature of meridional heat transport by transient eddies. *Quarterly Journal of the Royal Meteorological Society*, 139, 999–1008.
Messori, G. & Czaja, A. (2015) On local and zonal pulses of atmospheric heat transport in reanalysis data. *Quarterly Journal of the Royal Meteorological Society*, 141, 2376–2389.
Messori, G., Geen, R. & Czaja, A. (2017) On the spatial and temporal variability of atmospheric heat transport in a hierarchy of models. *Journal of the Atmospheric Sciences*, 74, 2163–2189.
Murray, R.J. & Simmonds, I. (1991) A numerical scheme for tracking cyclone centres from digital data. Part I: development and operation of the scheme. *Australian Meteorological Magazine*, 39, 155–166.
Nakamura, H., Sampe, T., Goto, A., Ohfuchi, W. & Xie, S.-P. (2008) On the importance of midlatitude oceanic frontal zones for the mean state and dominant variability in the tropospheric circulation. *Geophysical Research Letters*, 35, L15 709.
Neu, U., Akperov, M.G., Bellenbaum, N., Benestad, R., Blender, R., Caballero, R. et al. (2013) IMILAST: a community effort to intercompare extratropical cyclone detection and tracking algorithms. *Bulletin of the American Meteorological Society*, 94, 529–547.
Novak, L., Ambaum, M. & Tailleux, R. (2017) Marginal stability and predator–prey behaviour within storm tracks. *Quarterly Journal of the Royal Meteorological Society*, 143, 1421–1433.
Ogawa, F. & Spengler, T. (2024) Influence of mid-latitude sea surface temperature fronts on the atmospheric water cycle and storm track activity. *Weather and Climate Dynamics*, 5, 1031–1042.
Papritz, L. & Spengler, T. (2015) Analysis of the slope of isentropic surfaces and its tendencies over the North Atlantic. *Quarterly Journal of the Royal Meteorological Society*, 141, 3226–3238.
Parker, D. (1998) Secondary frontal waves in the North Atlantic region: a dynamical perspective of current ideas. *Quarterly Journal of the Royal Meteorological Society*, 124, 829–856.
Pfahl, S. & Wernli, H. (2012) Quantifying the relevance of cyclones for precipitation extremes. *Journal of Climate*, 25, 6770–6780.
Priestley, M.D., Ackerley, D., Catto, J.L., Hodges, K.I., McDonald, R.E. & Lee, R.W. (2020a) An overview of the extratropical storm tracks in CMIP6 historical simulations. *Journal of Climate*, 33, 6315–6343.
Priestley, M.D., Dacre, H.F., Shaffrey, L.C., Schemm, S. & Pinto, J.G. (2020b) The role of secondary cyclones and cyclone families for the North Atlantic storm track and clustering over western Europe. *Quarterly Journal of the Royal Meteorological Society*, 146, 1184–1205.
Renfrew, I.A., Barrell, C., Elvidge, A., Brooke, J., Duscha, C., King, J. et al. (2021) An evaluation of surface meteorology and fluxes over the Iceland and Greenland Seas in ERA5 reanalysis: the impact of sea ice distribution. *Quarterly Journal of the Royal Meteorological Society*, 147, 691–712.
Rivals, H., Cammas, J.-P. & Renfrew, I.A. (1998) Secondary cyclogenesis: the initiation phase of a frontal wave observed over the eastern Atlantic. *Quarterly Journal of the Royal Meteorological Society*, 124, 243–267.
Schemm, S. (2023) Toward eliminating the decades-old too zonal and too equatorward storm-track bias in climate models. *Journal of Advances in Modeling Earth Systems*, 15(2), e2022MS003482.
Shaw, T.A. (2019) Mechanisms of future predicted changes in the zonal mean mid-latitude circulation. *Current Climate Change Reports*, 5, 345–357.
Spensberger, C. (2024) Dynlib: a library of diagnostics, feature detection algorithms, plotting and convenience functions for dynamic meteorology. https://doi.org/10.5281/zenodo.10471187
Spensberger, C. & Marcheggiani, A. (2024) ERA5 cyclone tracks. https://doi.org/10.11582/2024.00023.
Spensberger, C. & Sprenger, M. (2018) Beyond cold and warm: an objective classification for maritime midlatitude fronts. *Quarterly Journal of the Royal Meteorological Society*, 144, 261–277.
Spensberger, C., Konstali, K. & Spengler, T. (2025) Moisture transport axes: a unifying definition for tropical moisture exports, atmospheric rivers, and warm moist intrusions. *Weather and Climate Dynamics*, 6, 431–446. Available from: https://doi.org/10.5194/wcd-6-431-2025.
Thomas, C.M. & Schultz, D.M. (2019) Global climatologies of fronts, airmass boundaries, and airstream boundaries: why the definition of front matters. *Monthly Weather Review*, 147, 691–717.
Weijenborg, C. & Spengler, T. (2020) Diabatic heating as a pathway for cyclone clustering encompassing the extreme storm Dagmar. *Geophysical Research Letters*, 47(8), e2019GL085777.
Wernli, H. & Schwierz, C. (2006) Surface cyclones in the ERA-40 dataset (1958–2001). Part I: Novel identification method and global climatology. *Journal of the Atmospheric Sciences*, 63, 2486–2507.
Willison, J., Robinson, W.A. & Lackmann, G.M. (2013) The importance of resolving mesoscale latent heating in the North Atlantic storm track. *Journal of the Atmospheric Sciences*, 70, 2234–2250.
Woollings, T., Papritz, L., Mbengue, C. & Spengler, T. (2016) Diabatic heating and jet stream shifts: A case study of the 2010 negative North Atlantic Oscillation winter. *Geophysical Research Letters*, 43, 9994–10002.

## SUPPORTING INFORMATION

Additional supporting information can be found online in the Supporting Information section at the end of this article.

**How to cite this article:** Marcheggiani, A., Dacre, H., Spensberger, C. & Spengler, T. (2025) Weather features drive free-tropospheric baroclinicity variability in the North Atlantic storm track. *Quarterly Journal of the Royal Meteorological Society*, e5061. Available from: https://doi.org/10.1002/qj.5061

## APPENDIX A. CYCLONE CENTRE DETECTION AND TRACKING ALGORITHM

To detect (and track) cyclones we use an algorithm based on Murray and Simmonds (1991). We first filter spatially SLP by spectral truncation at T84 to avoid numerical issues with small-scale noise in the SLP field. Then we detect maxima in the Laplacian of SLP and classify them as

- "closed" systems if a minimum in SLP is present within 500 km of the maximum Laplacian;
- "open" systems if not closed and within 500 km of a minimum in the SLP gradient.

Cyclones in their closed stage usually have a closed contour around their centre, making them more distinct compared with their open stage, when they might be embedded in a more or less active trough. The detection is carried out separately for the Northern and Southern Hemispheres on polar stereographic grids with a horizontal resolution of around 10 km in the $x$- and $y$-directions, allowing for a high precision in locating the centre of a cyclone. Cyclone centres are initially located at discrete grid points of these high-resolution grids, but these positions are subsequently refined as part of the cyclone tracking algorithm.

Once cyclone centres are detected, we track them in time using the best match between predicted cyclone positions and the actual detected positions. Cyclone movement is predicted using a Kalman filter, assuming a constant movement vector for the forecasting step. The Kalman state (cyclone position and movement) and its uncertainty are updated every new time step at which the cyclone is detected. To reflect that the movement vector is unknown before the second observation, the Kalman filter is initialised at a state of rest and with large uncertainty in the movement vector. We impose a maximum distance between predicted and detected cyclone positions of 750 km.

Once a track is completed, cyclone positions are updated using a Kalman smoother so that the best guess of cyclone position and movement in the final dataset is also based on detected positions at the following time steps.

Finally, tracks are filtered to discard spurious, weak, and short-lived features, requiring a minimum distance between the first and last points of each track of 500 km as well as a minimum lifetime of 24 hr. In addition, we retain only those systems that are closed at least once during their lifetime.

The winter climatology of these cyclone tracks (Figure A1) is in broad agreement with results from other widely used tracking algorithms, especially those also based on the Murray and Simmonds algorithm methods M02 and M10 in Neu *et al.*, 2013. The tracking algorithm in Python (as part of dynlib; Spensberger, 2024) and the actual tracks data (Spensberger & Marcheggiani, 2024) are publicly available.

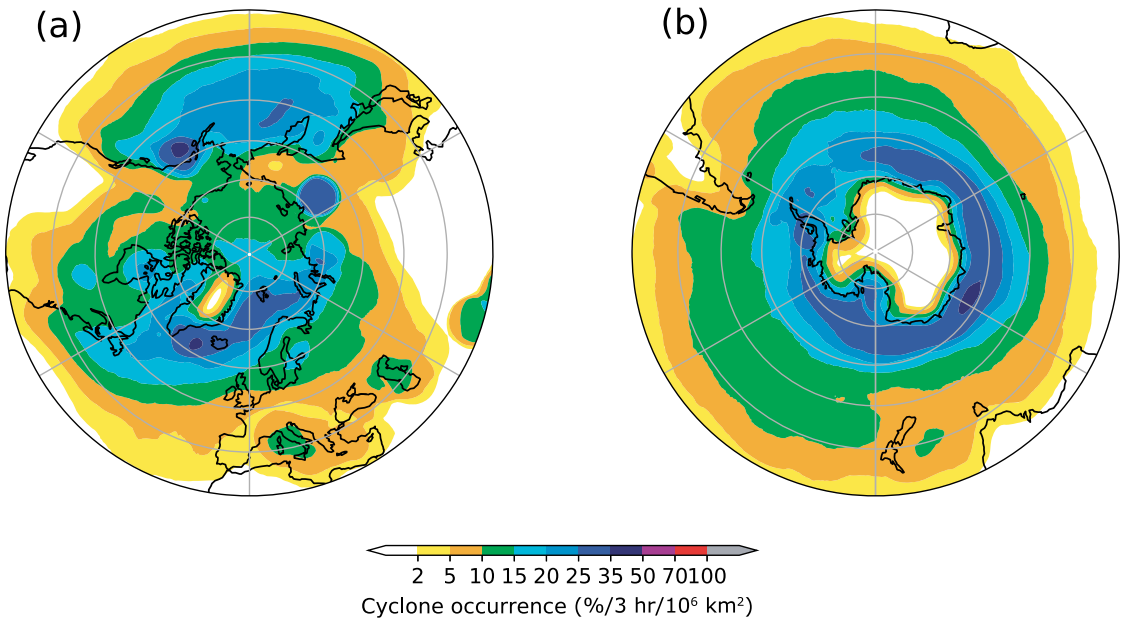


**FIGURE A1** Total cyclone centre density in the (a) Northern and (b) Southern Hemispheres for cyclones detected and tracked as described in Appendix A. Density is estimated as percentage of cyclone occurrence per time step (3 hr) and over an area of $10^6$ km$^2$. [Colour figure can be viewed at wileyonlinelibrary.com]